Chemo-mechanical evolution of pore space in carbonate microstructures upon dissolution: linking pore geometry to bulk elasticity

C. Arson,[1] and T. Vanorio,[2]

Corresponding author: C. Arson, School of Civil & Environmental Engineering, Georgia Institute of Technology, GA (chloe.arson@ce.gatech.edu)

[1]School of Civil & Environmental Engineering, Georgia Institute of Technology, GA, USA

[2]Stanford Rock Physics Laboratory, Stanford University, CA, USA

Abstract. One of the challenges faced today in a variety of geophysical applications is the need to understand the changes of elastic properties due to time-variant chemo-mechanical processes. The objective of this work is to model carbonate rock elastic properties as functions of pore geometry changes that occur when the solid matrix is dissolved by carbon dioxide. We compared two carbonate microstructures: porous micrite ("mudstone") and grain-supported carbonate ("packstone"). We formulated a mathematical model that distinguishes the effects of micro- and macro- porosity on stiffness changes. We used measures of mechanical and chemical porosity changes recorded during injection tests to compute elastic moduli and compare them to moduli obtained from wave velocity measurements. In mudstones, both experimental and numerical results indicate that bulk moduli change by less than 5%. The evolution of elastic moduli is controlled by macropore enlargement. In packstones, model predictions under-estimate changes of elastic moduli with total porosity by 10% to 80%. The total porosity variation is 60% to 75% smaller than the chemical porosity variation, which indicates that pore expansion due to dissolution is counter-balanced by pore shrinkage due to compaction. Packstone elastic properties are controlled by grain sliding. The methodology presented in this paper can be generalized to other chemo-mechanical processes studied in rocks, such as dislocations, glide, diffusive mass transfer, recrystallization and precipitation.

Keywords: carbonate; dissolution; microporosity; macroporosity; elasticity

1. Introduction

One of the challenges faced today in a variety of geophysical applications is the need to understand the changes of elastic properties due to time-variant diagenetic and metamorphic processes [*Ortoleva*, 1994; *Zhu et al.*, 1995; *Zhu and Wong*, 1997; *Evans et al.*, 1999]. Underlying pore deformation mechanisms are either purely mechanical (e.g., fracturing at Hertzian contacts, grain sliding) or chemo-mechanical (e.g., pressure solution, dissolution, precipitation and healing via solution transfer and consequent cementation, crystal plasticity and lattice dislocation, and hydrothermal reactions). Mechanical sediment consolidation and chemical microstructure changes are often treated separately, despite the coupling that has been observed between the two [*Scholz et al.*, 1995]. For instance, under a constant stress, dissolution lowers rock strength and leads to grain sliding and compaction [*Vanorio et al.*, 2014]. Chemical compaction is accomplished by solution-transfer [*Durney*, 1972]: dissolution at points of greatest stress (*i.e.*, grain contacts) and re-precipitation in lower-stress regimes in the adjacent pores. Organic maturation and thermochemical transformation of the mineral phase can create aggressive fluids charged with organic acid, carbon dioxide and hydrogen sulphide [*Mazzullo and Harris*, 1992], which may either reduce porosity through cementation and pressure solution [*de Meer and Spiers*, 1999], enhance pre-existing pores, or create new ones through cement dissolution and pore-pressure build-up [*Mazzullo et al.*, 1996].

Experiments performed in geochemistry and in rock physics are based on different types of material, parameters, scales of investigation, and pressure and temperature conditions. Studies of reaction mechanisms and kinetics focused on mineral powders, which allowed

understanding the influence of pressure, temperature and fluid composition [*Heinrich et al.*, 1989; *Tanner et al.*, 1985] as well as that of reactant surfaces and nucleation processes on reaction kinetics [*Dachs and Metz*, 1988; *Schramke et al.*, 1987; *Lüttge and Metz*, 1991]. However, models were not applicable to natural systems, due to the large porosities of the powders, the large surface areas of the mineral reactants, and the abundant fluid phases [*Lüttge and Metz*, 1993]. Moreover, experiments performed in a batch assume that the thermodynamic system under study is closed, which is of limited interest in Earth sciences [*Steefel and Maher*, 2009]. Experimental analogs were used in order to observe chemo-mechanical changes of pore geometry at a larger scale than that of actual rock pores. For instance, Sprunt and Nur [*Sprunt and Nur*, 1977] experimentally showed that a spherical hole drilled centrally within slabs of different materials increased in size because the solid matrix dissolved; the holes also flattened in the direction normal to compression stress, which implies a change in the stiffness of the hole. In a porous medium, pore space compressibility is defined as the ratio of the fractional change in pore volume, v_p, to an increment of applied mean stress σ [*Mavko and Mukerji*, 1998]:

$$\frac{1}{K_{dry}} = \frac{1}{K_s} + \underbrace{\frac{\Phi}{v_p}\frac{\partial v_p}{\partial \sigma}}_{\frac{\Phi}{K_\Phi}} \tag{1}$$

In which Φ is porosity and K_s is the bulk modulus of the solid grains. Vanorio et al. [*Vanorio et al.*, 2014] found that the pore space compressibility $1/K_\Phi$ of the original rock plays a key role in defining different styles of modifications of the pore network.

Gassmann's model [*Gassmann*, 1951] is used as a general basis for interpreting the effect of fluids on both log and seismic velocity data. Vanorio et al. [*Vanorio et al.*, 2014] emphasized that the model scheme performs a simple fluid substitution, predicting the

change in moduli and density of the rock by replacing one pore fluid with another, and then converting the predicted moduli and density back to velocities. In such a scheme, the rock-fluid interaction is treated as a purely mechanical problem: that is, the change in seismic velocity depends only on the compressibility and density of the fluid (ρ_{fl}; K_{fl}), the physical parameters controlling them [*Batzle and Wang*, 1992], and the density and elastic moduli of the rock frame (ρ_{dry}; K_{dry}; G_{dry}). It is a common practice in the literature to include the time-variant effects on the properties of the fluid and the rock frame due to the variation of physical parameters, such as stress and temperature, which respectively induce compaction and fluid-phase changes [*Nur and Thanh*, 1984; *Lumley*, 2001; *Guilbot and Smith*, 2002; *Hatchell and Bourne*, 2005; *Meadows et al.*, 2005]. A basic assumption of Gassmann's theory is that the fluid and the rock matrix do not interact, implying that, when this occurs *in situ*, the elastic moduli of the rock frame and its porosity are treated as time-invariant parameters in a 4D scheme. Several studies reported instances of a significant change in S-wave velocity associated with enhanced recovery operations and CO_2 injection, as well as time-lapse effects larger than those predicted by Gassmann's model [*Wang et al.*, 1998; *Guilbot and Smith*, 2002; *Davis et al.*, 2003; *Daley et al.*, 2008; *McCrank and Lawton*, 2009]. Inherently, Gassmann's modeling cannot account for a change in the shear modulus, which in turn leads to changes in S-wave velocity. To match the observed changes, there is no choice but to invoke changes in effective stress [*Wang et al.*, 1998; *Gritto and Myer*, 2004].

This study builds upon the experimental work of Vanorio et al. [*Vanorio et al.*, 2014], and aims to provide a modeling scheme to be used when a reactive fluid changes the pore space of a rock in response to microstructural adjustments as the fluid-rock system

attains a new chemo-mechanical equilibrium. To do so, we use microscopic observations from SEM images of pore dissolution and compaction in two carbonate microstructures, porous micrite ("mudstone") and grain-supported carbonate ("packstone"). We propose a homogenization scheme that relates carbonate elastic moduli to the most important geometric parameters of the microstructure identified in the experiments. Section 2 explains the experimental methods and modeling assumptions. Parametric studies are presented in Section 3. In Section 4, we compare model predictions of elastic moduli to experimental measurements, for the same porosity changes.

2. Methodology

2.1. Materials

Following Dunham's classification [*Dunham*, 1962], mudstone is defined as a matrix-supported carbonate rock that contains less than 10% of grains in the mud matrix (*i.e.*, microcrystalline calcite), whereas packstone is a grain-supported carbonate (*i.e.*, grainstone) that contains lime mud in the pore space. We used the experimental results reported in [*Vanorio et al.*, 2014] to constrain our model of carbonate stiffness evolution.

The depositional fabric of the mudstone samples corresponds to tight bioclastic carbonates ($\Phi \leq 10\%$) characterized by an interlocked mosaic of micritic matrix (Figure 1). The packstone samples come from a depositional sequence that is typical of a transgressive systems tract that vary from chalky, whitish grainstones with variable micrite content (Figure 2) [*Vanorio and Mavko*, 2011]. Packstone samples show larger porosity ranging from 20% to 30%.

2.2. Experimental procedure and Observations

The overall experiment, described in [*Vanorio et al.*, 2011, 2014], started with a baseline characterization of the samples' porosity through Helium porosimetry and ultrasonic P- and S- wave velocity under controlled pressure conditions. PZT- crystals mounted on steel endplates of the core holder were used to generate P- and S- waves (1 MHz for P-waves and 0.7 MHz for S-waves). Estimation of the accuracy in velocity and porosity was approximately $\pm 1\%$. During the experiment, the core plugs (1 in. diameter by approximately 1 in. length) were jacketed with rubber tubing to isolate them from the medium exerting confining pressure. As a first step, the samples were loaded up step-wise to a confining pressure of 15 MPa. During this stage, samples were dry, and P- and S- wave velocities were recorded along the loading pressure path (pre-injection measurements). Then, samples were injected with a pre-mixed, aqueous CO_2 solution while being under confining pressure and ambient temperature conditions. The flow-through experiment was subsequently performed by injecting volumes of fluid normalized by the sample pore volume, V_p. Pore pressure injection ranged between 10 MPa and 13 MPa. During injection, a constant downstream flow rate of 5 ml/min was maintained. The effective pressure ranged between 2 MPa and 5 MPa, depending on the trade-off between sample permeability and flow rate. Several cumulative injections were performed during each experimental run, up to $V_p \simeq 500$. The objective was to expose the samples to increasing V_p and to understand the role of the continued exposure on the trends of the measured elastic properties.

After each injection, Helium gas was injected through the sample for 8 hours to ensure drying within the vessel. This allowed measuring and monitoring the variation of the properties of the frame alone while minimizing the potential influence of fluids on wave

propagation, e.g. the attenuation related to Wave Induced Fluid Flow or Biot mechanism. After each flooding-drying cycle, samples' porosity and ultrasonic P- and S- wave velocity under pressure conditions were re-measured. The change in porosity was monitored by measuring two contributions: the loss in porosity due to compaction under stress and the enhancement of porosity from the dissolution of the frame and/or mechanical removal of particles occurring during injection [*Vanorio et al.*, 2011]. The former can be approximated by measuring the sample strain, while the latter comes from measuring the Ca and Mg cation concentration in the collected aqueous solution. To measure the strain, three linear potentiometers were used to measure length changes of the samples as a function of stress. The length changes were related to changes in porosity by assuming that pore contraction was the main cause of strain. The change in porosity due to dissolution was obtained from the concentration of cations by using the following formula:

$$\Delta\Phi_C(t_i) = \frac{\sum_j \Delta m_j}{V_{REV}\rho_s} = \Delta V_f(t_i)\frac{\sum_j C_j M_{w,j}}{V_{REV}\rho_s} \tag{2}$$

$\Delta\Phi_C(t_i)$ is the change in porosity calculated from the measured concentration of the dissolved cations over the period $[t_{i-1}, t_i]$, between two fluid samplings. V_{REV} is the volume of the sample (considered here as the Representative Elementary Volume, REV), ρ_s is the mass density of the REV solid skeleton (grain density). Δm_j is the change in mass due to the dissolution of the j^{th} mineral over the period $[t_{i-1}, t_i]$. The mass change is calculated from the mean concentration C_j of the dissolved cations from the j^{th} mineral, the molecular weight $M_{w,j}$ of the dissolving mineral species, and the volume of the injected fluid $V_f(t_i)$ (note: lab measurements of water hardness are in milligrams per liter and are equivalent to the product $C_j M_{w,j}$). The total net change in porosity is thus the resulting porosity from each component.

Upon sample recovery from the vessel, time-lapse SEM imaging of the samples was performed to relate changes in the measured physical properties to those in the rock microstructure. Different imaging magnifications of the sample allowed different scales of observation, from micro- to macro- scale, that are used to inform the modeling strategy. Observations refer to changes with respect to the properties of initial microstructures, summarized in Tables 1 and 2. In tight mudstones (Figure 1), the shape and size of macropores are not significantly affected by dissolution and compaction (Figure 1(D)). Nevertheless, at higher magnifications, the microstructure shows an increase in microporosity (Figure 1(B)). Such an increase results from the decrease in size of the micrite grains, which are dissolved during the injection because of the higher surface area of this crystalline phase. In addition, as hypothesized in [*Vanorio et al.*, 2014], the low permeability of the sample favors a poor dewatering of the Ca^{2+} ion-rich water, leading to supersaturation. In turns, this leads calcite to precipitate and weld micro-grains together under the effect of pressure. As a result, micropores are either enlarged by dissolution or cemented by precipitation (Figure 1(B)). The direct consequence of these processes is that the enhancement of pore throats together with cementation does not contribute much to the total porosity or to the decrease in velocity. Porosity changes were half ($\simeq 2pu$) of those measured in packstone, and velocity variations were less than 5%. Total porosity changes were similar to chemical porosity changes (calculated from mass changes) since negligible pore compaction was observed. Vanorio et al. [*Vanorio et al.*, 2014] hypothesized that the change in velocity is controlled by a change in pore stiffness, i.e., a change in pore shape. This phenomenon can be explained by the the fact that stress around pores is not uniformly distributed due to the presence of rock heterogeneities. Dissolution

first takes place at points of high stress concentrations, which can result in pore shape changes [*Lecampion*, 2010].

Conversely, the presence of the high-surface-area, micrite phase filling the macropores of the micrite-rich packstones samples (Figure 2(A)) leads to a different evolution of the microstructure upon injection, and hence of its elastic properties. At higher magnification, the evolution of the tight micrite porous matrix is similar to that observed in the microstructure of tight mudstones (Figure 2(D)), showing minimal changes. Nevertheless, at lower magnification, the images show that macro porosity increases at the expense of the porous micrite aggregates that are both dissolved and mechanically removed from pores upon injection (Figure 2(B)). The comparison between Figure 2(A) (before injection) and Figure 2(B) (after injection) highlights two main changes: 1) a more porous microstructure exists after injection manifesting itself as pores free of micrite and 2) the sample experiences compaction due to slippage and/or local rearrangement of grains accommodating the dissolution of cement and micrite. Vanorio et al. [*Vanorio et al.*, 2014] hypothesized that dissolution-induced compaction ultimately reduces the stiffness at the grain contacts. If contacts are not promptly re-cemented, the velocity of the rock framework is permanently reduced as fluid circulation proceeds. Injection was found to have a negligible effect on larger grains (Figure 2(B)) that are present in the microstructure because of micrite dissolution. Therefore, in the model proposed herein, we assumed that larger calcite grains keep the same size.

Time-lapse images indicated changes with respect to the initial microstructure that were visible throughout the sample, from the top (Figures 2(A-B)) to the bottom (Figures 2(C-D)) where smaller micritic particles have disappeared and pits of dissolution have been

created on the grain surfaces. This observation implies that, though the fluid is buffered while travelling though the sample, the reaction front advanced at each injection, reaching the bottom of the sample. CT scan observations performed to compare rock volumes before and after injection showed that dissolution was highly heterogeneous [*Vanorio et al.*, 2011], even when the volumetric flux was sufficient to guarantee both a low Peclet number (Pe) and a low product (less than 1) of the Peclet and Damkohler numbers (PeDa). Kang et al. [*Kang et al.*, 2003] showed that when both Pe and PeDa are less than 1, the dissolution process is reaction-limited, which results in a uniform dissolution over all the solid walls. Vanorio et al. [*Vanorio et al.*, 2011] attributed the selective dissolution to the heterogeneity of the starting microstructures, from mud- to grain- supported fabrics, controlling both the overall surface area of the samples and its permeability.

2.3. Modeling Strategy

Based on the observations presented in Tables 1 and 2, we modeled mudstone (medium "M2") as a mixture made of spherical macro-pores ("MaP," about 10 μm in size) embedded in a porous micrite matrix (medium "M1") containing spherical micro-pores ("MiP," about 2-5 μm in size) and micrite grains ("Mic," 4-6 μm in size). We modeled packstone (medium "P3") as a mixture of tubular macro-pores ("T") embedded in a porous skeleton (medium "P2"), made of large calcite grains ("Cal," a few hundreds of microns in size), micrite grains and micropores. We calculated the elastic moduli of mudstone and packstone by homogenization. The main assumptions and computation steps are summarized in Tables 3 and 4, and detailed in the following.

We determined the bulk and shear moduli of the porous micrite matrix (medium M1) by applying the self-consistent method [*Berryman*, 1980], in which micrite grains are con-

sidered as spherical elements, and micropores are considered as randomly oriented oblate spheroids (axes of dimensions $a = b > c$). Note that before CO_2 injection, micropores are assumed to be spherical (Table 3). The equations of the model are reported in Appendix A. We determined the bulk and shear moduli of mudstone (medium M2) by applying the self-consistent method a second time (Appendix A), in which elements of porous micrite matrix (medium M1) are considered as spherical, and macropores are considered as randomly oriented oblate spheroids (axes of dimensions $a = b > c$), initially spherical before CO_2 injection (Table 3). The bulk and shear moduli of mudstone macropores (noted $K_{\Phi_{MaP}}$ and $G_{\Phi_{MaP}}$) are the stiffness coefficients of oblate spheroidal inclusions, which can be expressed as follows [*Mavko et al.*, 2009]:

$$K_{\Phi_{MaP}} = \frac{3\pi\, K_{M1}\,(1-2\nu_{M1})}{4(a_{MaP}/c_{MaP})(1-{\nu_{M1}}^2)} \tag{3}$$

$$G_{\Phi_{MaP}} = \frac{\pi\, G_{M1}\,(2-\nu_{M1})}{2(a_{MaP}/c_{MaP})(1-\nu_{M1})} \tag{4}$$

In which c_{MaP}/a_{MaP} refers to the aspect ratio of macro pores, and ν_{M1} is the Poisson's ratio of the porous micrite matrix (medium M1).

In a former study [*Vanorio and Mavko*, 2011], packstone elastic moduli were obtained by applying the self-consistent method twice: once for the microporous micrite matrix P1 (in the same way as for medium M1 above), and once for a mixture made of microporous matrix (P1), calcite grains and macropores. The elastic moduli were then fitted to measures of wave velocity changes. The aspect ratio of macropores was estimated to be $c_{MaP}/a_{MaP} = 0.08$. As explained in Section 2, we modeled macropores as tubes with a cross section typical of inter-granular spaces. We calculated the bulk and shear moduli of packstone in three steps (Table 4). We used the same homogenization procedure as in

mudstone to obtain the elastic moduli of the micrite porous matrix in packstone (medium P1 = medium M1). Then we obtained the elastic properties of the skeleton of packstone (medium P2 = mixture of medium M1 and calcite grains) by applying the self consistent method a second time (details are provided in Appendix A). Macropores embedded in the solid skeleton of packstone were modeled as tubes of finite length lying between grain edges, as illustrated in Figure 3a. The position of the points that form the contour of the cross-section of such tubes can be parametrized in an (x, y) coordinate system, according to the following equations [*Mavko et al.*, 2009]:

$$x = R_0\left(cos\theta + \frac{1}{2+\gamma}cos2\theta\right)$$

$$y = R_0\left(sin\theta + \frac{1}{2+\gamma}sin2\theta\right)$$

In which γ is a roundness parameter (Figure 3b). Calcite and micrite grains are assumed to be spherical; therefore, the geometry of the interstitial space between grain edges is assumed to be best represented by the shape parametrized by $\gamma = 0$. In this case, Mavko [*Mavko*, 1980] showed that:

$$\frac{1}{K_{\Phi_{MaP}}} = \frac{1}{K_{P2}} \cdot \frac{13 - 4\nu_{P2} + 8(\nu_{P2})^2}{3(1-2\nu_{P2})} \tag{5}$$

$$\frac{1}{G_{\Phi_{MaP}}} = \frac{1}{G_{P2}} \cdot \frac{2(40 - 26\nu_{P2})}{15} \tag{6}$$

In which K_{P2} and ν_{P2} are the bulk modulus and Poisson's ratio of packstone skeleton (medium P2), respectively. Like micropores, macropores are assumed to conserve the same kind of shape upon dissolution and compaction, so that Eq. 5-6 remain valid even when macro porosity changes during the reactive flow through experiment. Packstone

elastic properties are obtained by using Equation 1:

$$\frac{1}{K_{P3}} = \frac{1}{K_{P2}} + \frac{\Phi_{MaP}}{K_{\Phi_{MaP}}} \tag{7}$$

$$\frac{1}{G_{P3}} = \frac{1}{G_{P2}} + \frac{\Phi_{MaP}}{G_{\Phi_{MaP}}} \tag{8}$$

3. Results

3.1. Variations of mudstone stiffness with micro- and macro- porosity

Parametric studies were conducted with the model presented above. Figures 4 and 5 show the evolution of the elastic moduli of the porous micrite matrix (medium M1) with microporosity and the evolution of the pores' aspect ratio (c/a) upon dissolution. Figures 6a-6b show the variations of mudstone elastic moduli with microporosity and macro porosity. For a mudstone with an initial microporosity of 10% and an initial macro porosity of 1%, a 10% increase in microporosity (at constant macroporosity) makes the bulk modulus drop by more than 30%, and a 10% increase in macroporosity (at constant microporosity) makes the bulk modulus drop by 15%. Upon dissolution, the shape of macro pores evolves from a sphere to an oblate spheroid (more compliant than a sphere) and the stiffness of the micrite porous matrix decreases because microporosity increases (Figure 7).

3.2. Variations of packstone stiffness with micro- and macro- porosity

In packstone, the increase of microporosity that occurs upon dissolution reduces the moduli of the porous micrite matrix (P1=M1) and those of packstone porous skeleton (P2), as illustrated in Figures 8a-8b. P2 elastic moduli are higher than P1 elastic moduli due to the presence of calcite grains. For instance, for a microporosity of 20%, the bulk

and shear moduli of P1 are 20% lower than those of P2. We verified that the composite moduli of P2 remains within Hashin-Shtrikman bounds. Because the P2 mixture contains calcite grains that are stiffer than medium P1, the elastic moduli of medium P1 are always inferior to P2 lower bound. Figure 9 shows that an increase of microporosity results in an increase of macropore compressibility, both because the volume of micropores increases and because the compressibility of micropores increases (due to the decrease in aspect ratio). Figures 10a-10b show the variations of packstone elastic moduli with microporosity and macroporosity.

4. Comparison with laboratory data and Discussion

4.1. Comparison between numerical predictions and experimental results

In the following we compare the elastic moduli obtained from wave velocity measurements to those predicted by our stiffness model, for the same porosity changes and initial conditions as in the experiments (Table 5). The comparison is aimed to assess the performance of the model to predict microstructure evolution from elastic properties. Numerical predictions were compared to experimental results for two end cases: (a) when the total porosity variation measured during the tests is attributed to a change of micropore volume fraction only; and (b) when the total porosity variation measured during the tests is attributed to a change of macropore volume fraction only. In the absence of detailed experimental data on mudstone initial microstructure, the sensitivity of elastic moduli to micro- and macro- porosity variations was analyzed with different ratios of initial microporosity to macroporosity, as indicated in Table 5.

4.2. Discussion of the model for mudstone

Figure 11 shows the variations of mudstone bulk modulus with porosity changes. Similar trends were obtained for the shear modulus (not shown here for the sake of brevity). Note that the negative variation of total porosity measured in one of the mudstone samples is due to precipitation and clogging. The decrease in bulk modulus measured in the mudstone samples during the flow through experiments never exceeded 5% of the initial elastic modulus. The total porosity variations measured at the different stages of the injection are equal to the chemical porosity variations, which confirms the quasi absence of pore compaction. The relative variation of porosity is of the order of 10%, with an initial porosity that never exceeds 50%, which corresponds to a maximum absolute change of porosity of 5%. The corresponding variations of mudstone elastic moduli fall in the range of experimental errors ($\pm 5\%$); therefore, the injection test results cannot be used to constrain the model and infer the evolution of microstructure. Nevertheless, it can be noted that for the range of porosity variations measured experimentally, the maximum change in elastic moduli predicted by the model is of the order of 5%, which is in agreement with the wave velocity measurements recorded during the injection tests. A statistical dataset of pore size, specific surface and connectivity is needed to understand the conditions in which porosity changes are dominated by dissolution or compaction.

4.3. Discussion of the model for packstone

Figures 12a and 12b show the influence of total and chemical porosity changes on the bulk and shear moduli of packstone. Total porosity changes were less than the chemical porosity changes, which confirmed that pore enlargement by dissolution was counterbalanced by pore shrinkage consequent to skeleton compaction. We calculated the varia-

tions of elastic moduli corresponding to the porosity increase measured in the experiments. If we assume that only microporosity (respectively, macroporosity) varies, variations of elastic moduli predicted by the model amount to 10 to 30% (respectively, 20 to 80 %) of the variations of elastic moduli calculated from wave velocity measurements. Therefore, the model does not capture the net porosity change, defined as the sum of chemical porosity change (positive) and mechanical porosity change (negative). It is hypothesized that microstructure changes are due to the dissolution of micrite at grain contacts, which could decrease wave velocity and elastic moduli, even for net porosity changes ranging between 5 and 10%.

5. Conclusions

In this paper, we proposed a multi-scale computational procedure to express mudstone and packstone elastic moduli as functions of microstructure descriptors identified in SEM observations. Descriptors include micro-porosity, macro-porosity, and pore aspect ratio. We plotted the variations of elastic moduli against the total and chemical porosity changes measured during flow through experiments. In mudstones, bulk moduli changed by less than 5%. This trend was well-captured by the model. In packstones, the total porosity variation was 60% to 75% smaller than the chemical porosity variation, which shows that pore expansion due to dissolution was counter-balanced by pore shrinkage due to compaction. The changes of bulk and shear moduli with total porosity were underestimated by 10% to 80% in the model predictions. The comparison between experimental and numerical results indicates that elastic property changes are controlled by macropore enlargement in mudstones, and by grain sliding in packstones.

348 The model can be used to relate the evolution of carbonate elastic moduli with that of
349 macro- and micro- porosities, which influence the magnitude and rate of stiffness changes
350 upon dissolution and compaction. Similarly to experimental data, model trends clearly
351 highlight that (1) the depositional-inherited microstructure plays a fundamental role in the
352 evolution of rock properties and (2) that the determination of macro- and micro-porosity
353 variations is key to properly inform modeling schemes in carbonates.

354 The methodology presented in this paper can be generalized to other chemo-mechanical
355 processes studied in rocks, such as dislocations, glide, diffusive mass transfer, recrystal-
356 lization and precipitation.

Appendix A: Equations used in the self-consistent method

357 We determined the bulk and shear moduli of the porous micrite matrix (medium M1)
358 by applying the self-consistent method [*Berryman*, 1980]:

$$359 \quad (K_{M1})_{n+1} = \frac{\Phi_{(2)} \times K_{(2)} \times (P^*)_n^{(2)} + (1-\Phi_{(2)}) \times K_{(1)} \times (P^*)_n^{(1)}}{\Phi_{(2)} \times (P^*)_n^{(2)} + (1-\Phi_{(2)}) \times (P^*)_n^{(1)}} \tag{A1}$$

$$360 \quad (G_{M1})_{n+1} = \frac{\Phi_{(2)} \times G_{(2)} \times (Q^*)_n^{(2)} + (1-\Phi_{(2)}) \times G_{(1)} \times (Q^*)_n^{(1)}}{\Phi_{(2)} \times (Q^*)_n^{(2)} + (1-\Phi_{(2)}) \times (Q^*)_n^{(1)}} \tag{A2}$$

361 The micrite porous matrix is denoted as "medium M1", in which constituent 1 is micrite
362 grains ($K_{(1)} = K_{CaCO3}$, $G_{(1)} = G_{CaCO3}$) and constitutent 2 is micropores ($K_{(2)} = 0$,
363 $G_{(2)} = 0$). $\Phi_{(2)}$ is the volumetric fraction of constituent 2 in medium M1. $(P^*)^{(1)}$ and
364 $(Q^*)^{(1)}$ are the "P and Q coefficients" of constituent 1 (micrite grains). $(P^*)^{(2)}$ and $(Q^*)^{(2)}$
365 are the "P and Q coefficients" of constituent 2 (micropores). Micrite grains are considered
366 as spherical elements, and micropores are considered as randomly oriented oblate spheroids

(axes of dimensions $a = b > c$). Therefore:

$$(P^*)^{(1)} = \frac{K_{M1} + \frac{4}{3}G_{M1}}{K_{(1)} + \frac{4}{3}G_{M1}} \tag{A3}$$

$$(Q^*)^{(1)} = \frac{G_{M1} + F_{M1}}{G_{(1)} + F_{M1}}, \quad F_{M1} = \frac{G_{M1}}{6}\left[\frac{9K_{M1} + 8G_{M1}}{K_{M1} + 2G_{M1}}\right] \tag{A4}$$

$$(P^*)^{(2)} = \frac{F_1}{F_2} \tag{A5}$$

$$(Q^*)^{(2)} = \frac{1}{5}\left[\frac{2}{F_3} + \frac{1}{F_4} + \frac{F_4F_5 + F_6F_7 - F_8F_9}{F_2F_4}\right] \tag{A6}$$

In which F_1,..., F_9 are functions of $K_{(1)}$, $G_{(1)}$ and the aspect ratio $\alpha = c/a$ (with $a > c$). Detailed expressions of F_1,..., F_9 are provided in the appendix of [*Berryman*, 1980] and are not repeated here. We note Φ_{micro} and Φ_{macro} the microporosity and macroporosity, respectively. We have: $\Phi_{micro} = (1 - \Phi_{macro}) \times \Phi_{(2)}$.

We determined the bulk and shear moduli of mudstone (medium M2) by applying the self-consistent method a second time. Constituent 1 was medium M1, and constituent 2 was macropores. Therefore we applied formulas A1-A6, in which we replaced the $M1$ subscript by the $M2$ subscript, and in which $\Phi_{(2)}$ is the volumetric fraction of macropores in medium M2 (mudstone), with $K_{(1)} = K_{M1}$, $G_{(1)} = G_{M1}$, $K_{(2)} = 0$, $G_{(2)} = 0$. In this second computational step, $(P^*)^{(1)}$ and $(Q^*)^{(1)}$ are the "P and Q coefficients" of constituent 1 (medium M1, micrite porous matrix). $(P^*)^{(2)}$ and $(Q^*)^{(2)}$ are the "P and Q coefficients" of constituent 2 (macropores). The elements of micrite porous matrix are considered as spherical, and macropores are considered as randomly oriented oblate spheroids (axes of dimensions $a = b > c$).

Similarly, for the skeleton of packstones (medium P2), we applied formulas A1-A2, in which we replaced the $M1$ subscript by the $P2$ subscript, and in which $\Phi_{(2)}$ is the volumetric fraction of constituent 2 (medium P1) in medium P2, with $K_{(1)} = K_{CaCO3}$,

$G_{(1)} = G_{CaCO3}$, $K_{(2)} = K_{P1}$, $G_{(2)} = G_{P1}$. In this homogenization scheme, $(P^*)^{(1)}$ and $(Q^*)^{(1)}$ are the "P and Q coefficients" of constituent 1 (calcite grains). $(P^*)^{(2)}$ and $(Q^*)^{(2)}$ are the "P and Q coefficients" of constituent 2 (medium P1). Calcite grains and elements of micrite porous matrix were assumed to remain spherical upon dissolution and compaction, therefore $(P^*)^{(1)}$, $(Q^*)^{(1)}$, $(P^*)^{(2)}$ and $(Q^*)^{(2)}$ were calculated by means of formulas A3-A4.

Acknowledgments. Upon request, the authors can provide all data necessary to understand, evaluate, replicate, and build upon the reported research.

References

Arson, C., and J.-M. Pereira (2013), Influence of damage on pore size distribution and permeability of rocks, *International Journal for Numerical and Analytical Methods in Geomechanics*, *37*, 810–831.

Arson, C., H. Xu, and F. Chester (2012), On the definition of damage in time-dependent healing models for salt rock, *Géotechnique Letters*, *2*, 67–71.

Batzle, M., and Z. Wang (1992), Seismic properties of pore fluids, *Geophysics*, *57*(11), 1396–1408.

Berryman, J. G. (1980), Long-wavelength propagation in composite elastic media: Ii. ellipsoidal inclusions, *J. Acoust. Soc. Am.*, *68*, 1820–1831.

Chadam, J., D. Hoff, E. Merino, P. Ortoleva, and A. Sen (1986), Reactive infiltration instabilities, *IMA Journal of Applied Mathematics*, *36*(3), 207–221.

Dachs, E., and P. Metz (1988), The mechanism of the reaction 1 Tremolite + 3 Calcite + 2 Quartz = 5 Diopside+ 3 CO_2 + 1 H_2O: results of powder experiments, *Contributions to Mineralogy and Petrology*, *100*(4), 542–551.

Daley, T. M., L. R. Myer, J. Peterson, E. Majer, and G. Hoversten (2008), Time-lapse crosswell seismic and vsp monitoring of injected co2 in a brine aquifer, *Environmental Geology*, *54*(8), 1657–1665.

Davis, T., M. Terrell, and R. Benson (2003), Multi-component seismic characterization and monitoring of the co2 flood at weyburn field, *The Leading Edge*, pp. 696–697.

de Meer, S., and C. J. Spiers (1999), On mechanisms and kinetics of creep by intergranular pressure solution, in *Growth, Dissolution and Pattern Formation in Geosystems*, pp. 345–366, Springer.

Dewers, T., and P. J. Ortoleva (1989), Mechano-chemical coupling in stressed rocks, *Geochimica et Cosmochimica Acta*, *53*(6), 1243–1258.

Dunham, R. J. (1962), Classification of carbonate rocks according to depositional textures, *Bulletin of the AAPG*.

Durney, D. (1972), Solution-transfer, an important geological deformation mechanism, *Nature*, *235*, 315–317.

Evans, B., Y. Bernabé, and W. Zhu (1999), Evolution of pore structure and permeability of rocks in laboratory experiments, in *Growth, Dissolution and Pattern Formation in Geosystems*, pp. 327–344, Springer.

Gassmann, F. (1951), Ueber die elastizitaet poroeser medien, *Vierteljahrsschrift der Naturforschenden Gesellschaft Zuerich*, *96*, 1–23.

Gritto, D. T. M., R., and L. Myer (2004), Joint cross-well and single-well seismic studies at lost hills, california, *Geophys. Prospect*, *52*, 323–339.

Guilbot, J., and B. Smith (2002), 4-d constrained depth conversion for reservoir compaction estimation: Application to ekofisk field, *The Leading Edge*, *21*(3), 302–308.

Hatchell, P., and S. Bourne (2005), Rocks under strain: Strain-induced time-lapse time shifts are observed for depleting reservoirs, *The Leading Edge*, *24*(12), 1222–1225.

Heinrich, W., P. Metz, and M. Gottschalk (1989), Experimental investigation of the kinetics of the reaction 1 Tremolite+ 11 Dolomite $\longleftrightarrow$ 8 Forsterite+ 13 Calcite+ 9 C_2 + 1 H_2O, *Contributions to Mineralogy and Petrology*, *102*(2), 163–173.

Kang, Q., D. Zhang, and S. Chen (2003), Simulation of dissolution and precipitation in porous media, *Journal of Geophysical Research: Solid Earth (1978–2012)*, *108*(B10).

Lecampion, B. (2010), Stress-induced crystal preferred orientation in the poromechanics of in-pore crystallization, *Journal of the Mechanics and Physics of Solids*, *58*(10), 1701–1715.

Lumley, D. E. (2001), Time-lapse seismic reservoir monitoring, *Geophysics*, *66*(1), 50–53.

Lüttge, A., and P. Metz (1991), Mechanism and kinetics of the reaction 1 Dolomite + 2 Quartz = 1 Diopside+ 2 CO_2 investigated by powder experiments, *The Canadian Mineralogist*, *29*(4), 803–821.

Lüttge, A., and P. Metz (1993), Mechanism and kinetics of the reaction: 1 Dolomite + 2 Quartz = 1 Diopside+ 2 CO_2: a comparison of rock-sample and of powder experiments, *Contributions to Mineralogy and Petrology*, *115*(2), 155–164.

Mavko, G., and T. Mukerji (1998), Bounds on low-frequency seismic velocities in partially saturated rocks, *Geophysics*, *63*(3), 918–924.

Mavko, G., T. Mukerji, and J. Dvorkin (2009), *The Rock Physics Handbook - Tools for Seismic Analysis of Porous Media, Second edition*, Cambridge University Press.

Mavko, G. M. (1980), Velocity and attenuation in partially molten rocks, *Journal of Geophysical Research: Solid Earth (1978–2012)*, *85*(B10), 5173–5189.

Mazzullo, S., and P. Harris (1992), Mesogenetic dissolution: its role in porosity development in carbonate reservoirs (1), *AAPG bulletin*, *76*(5), 607–620.

Mazzullo, S., H. Rieke, and G. Chilingarian (1996), *Carbonate Reservoir Characterization: A Geologic-Engineering Analysis, Part II: A Geologic-Engineering Analysis*, vol. 44, Elsevier.

McCrank, J., and D. C. Lawton (2009), Seismic characterization of a co 2 flood in the ardley coals, alberta, canada, *The Leading Edge*, *28*(7), 820–825.

Meadows, M., D. Adams, R. Wright, A. Tura, S. Cole, and D. Lumley (2005), Rock physics analysis for time-lapse seismic at schiehallion field, north sea, *Geophysical prospecting*, *53*(2), 205–213.

Nur, C. T., A. M., and D. V. Thanh (1984), Seismic monitoring of thermal enhanced oil processes, in *Proceedings of the 54th Annual International Meeting, SEG, Expanded Abstracts.*

Ortoleva, P., E. Merino, C. Moore, and J. Chadam (1987), Geochemical self-organization i: reaction-transport feedbacks and modeling approach, *Am. J. Sci*, *287*(10), 979–1007.

Ortoleva, P. J. (1994), *Geochemical self-organization*, Oxford University Press: Clarendon Press.

Pereira, J.-M., and C. Arson (2013), Retention and permeability properties of damaged porous rocks, *Computers & Geotechnics*, *48*, 272–282.

Scholz, C. H., A. Léger, and S. L. Karner (1995), Experimental diagenesis: Exploratory results, *Geophysical research letters*, *22*(6), 719–722.

Schramke, J. A., D. M. Kerrick, and A. C. Lasaga (1987), The reaction muscovite+ quartz $\longleftrightarrow$ andalusite+ k-feldspar+ water; part 1, growth kinetics and mechanism, *American*

Journal of Science, *287*(6), 517–559.

Sprunt, E., and A. Nur (1977), Experimental study of effects of stress on solution rate, *Journal of Geophysical Research*, *82*(20), 3013–3022.

Steefel, C. I., and K. Maher (2009), Fluid-rock interaction: A reactive transport approach, *Reviews in mineralogy and geochemistry*, *70*(1), 485–532.

Tanner, S., D. Kerrick, and A. Lasaga (1985), Experimental kinetic study of the reaction; calcite+ quartz $\longleftrightarrow$ wollastonite+ carbon dioxide, from 1 to 3 kilobars and 500 degrees to 850 degrees c, *American Journal of Science*, *285*(7), 577–620.

Vanorio, T., and G. Mavko (2011), Laboratory measurements of the acoustic and transport properties of carbonate rocks and their link with the amount of microcrystalline matrix, *Geophysics*, *76*(4), E105–E115.

Vanorio, T., A. Nur, and Y. Ebert (2011), Rock physics analysis and time-lapse rock imaging of geochemical effects due to the injection of co_2 into reservoir rocks, *Geophysics*, *76*(5), 23–33.

Vanorio, T., Y. Ebert, and D. Grombacher (2014), *What Laboratory-Induced Dissolution Tell us About Natural Diagenetic Trends of Carbonate Rocks (DOI 10.1144/SP406.4)*, Geological Society, London Special Publications, Agar, S. M. and Geiger, S. (eds).

Wang, Z., M. E. Cates, and R. T. Langan (1998), Seismic monitoring of a co2 flood in a carbonate reservoir: A rock physics study, *Geophysics*, *63*(5), 1604–1617.

Zhu, C., and C. Arson (2014a), A thermo-mechanical damage model for rock stiffness during anisotropic crack opening and closure, *Acta Geotechnica*, pp. DOI: 10.1007/s11,440–013–0281–0 (in press).

Zhu, C., and C. Arson (2014b), A model of damage and healing coupling halite thermo-mechanical behavior to microstructure evolution, *Geotechnical and Geological Engineering, Special Issue: Thermo-hydro-mechanical behavior of soils and energy geostructures*, p. (under review).

Zhu, W., and T.-f. Wong (1997), The transition from brittle faulting to cataclastic flow: Permeability evolution, *Journal of Geophysical Research: Solid Earth (1978–2012)*, *102*(B2), 3027–3041.

Zhu, W., C. David, and T.-f. Wong (1995), Network modeling of permeability evolution during cementation and hot isostatic pressing, *Journal of Geophysical Research: Solid Earth (1978–2012)*, *100*(B8), 15,451–15,464.

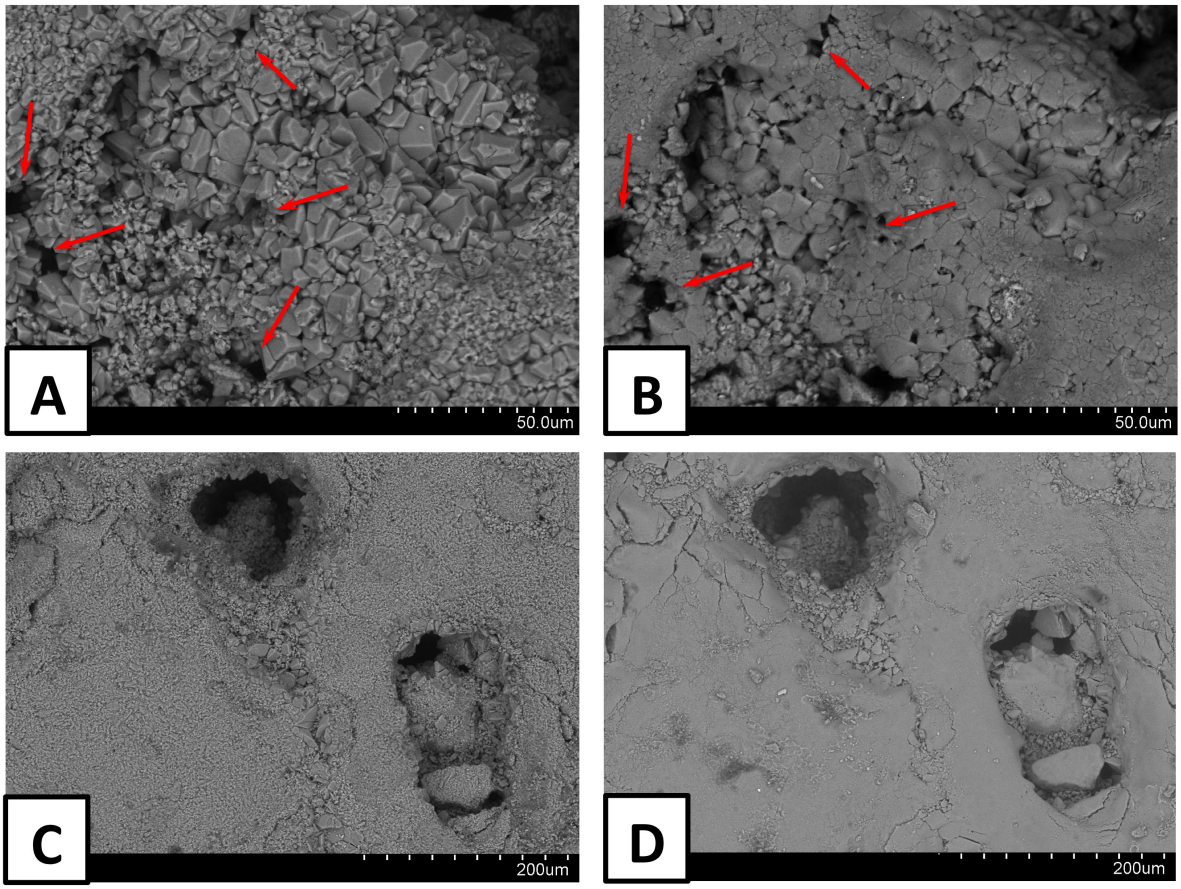

Figure 1. Evolution of mudstone microstructure upon dissolution and compaction. A-B: Enlargement of micropores embedded in the micrite porous matrix (A: before injection; B: after injection). Red arrows indicate the dissolution of micrite. C-D: Cementation of micropores embedded in the micrite porous matrix, by precipitation (C: before injection; D: after injection).

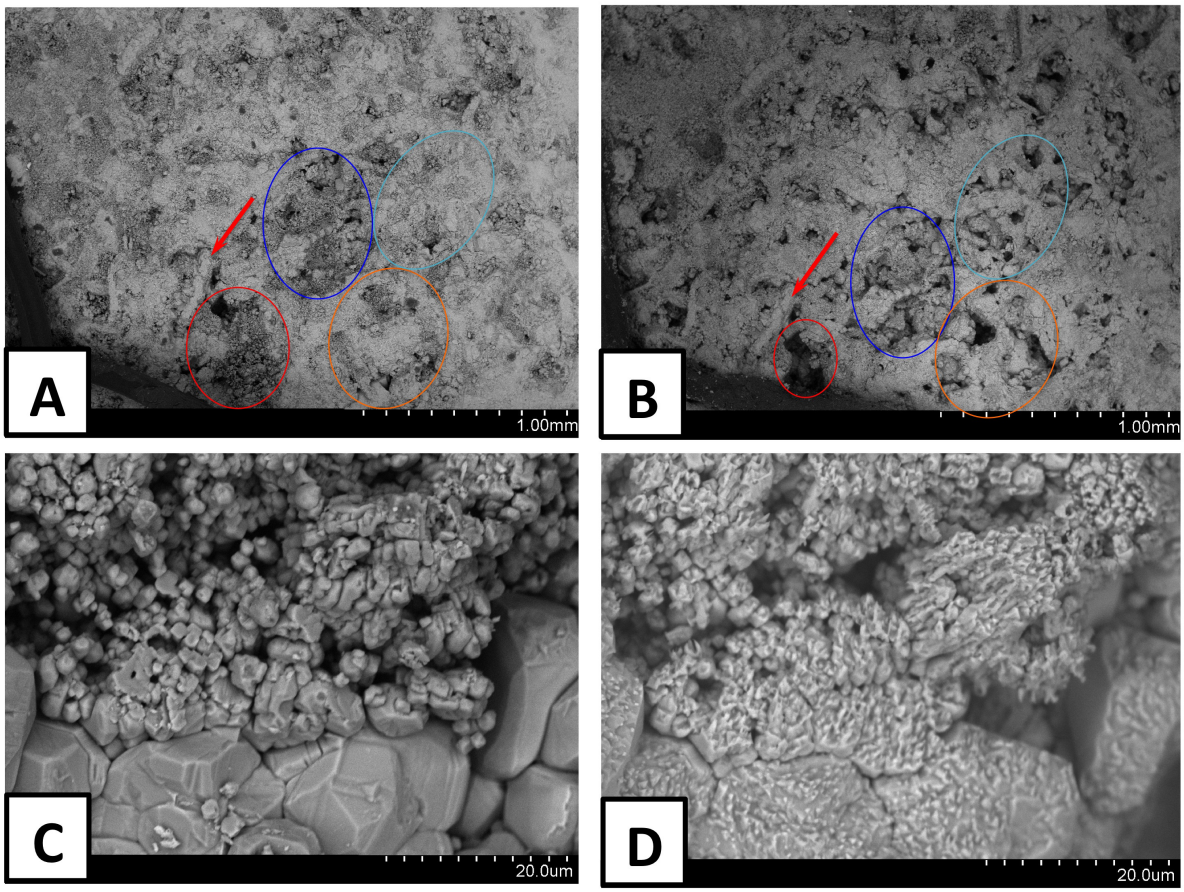

Figure 2. Evolution of packstone microstructure upon dissolution and compaction. A-B: Micrite porous matrix (A: before injection; B: after injection). Circles highlight areas of the samples showing dissolution of microcrystalline calcite (i.e., micrite) that enhances macro-porosity. In addition dissolution of micrite leads to compaction and topological re-arrangement of grains (red arrow and red circle). C-D: Large calcite grains and micrite porous matrix (C: before injection: D: after injection).

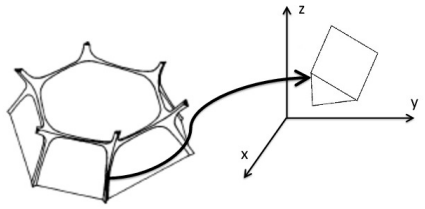

Figure 3a. Geometry of large pores embedded in packstone solid skeleton. Finite tubes along grain edges in 3D.

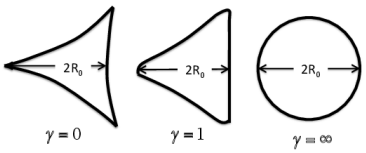

Figure 3b. Geometry of large pores embedded in packstone solid skeleton. Possible tube cross sections.

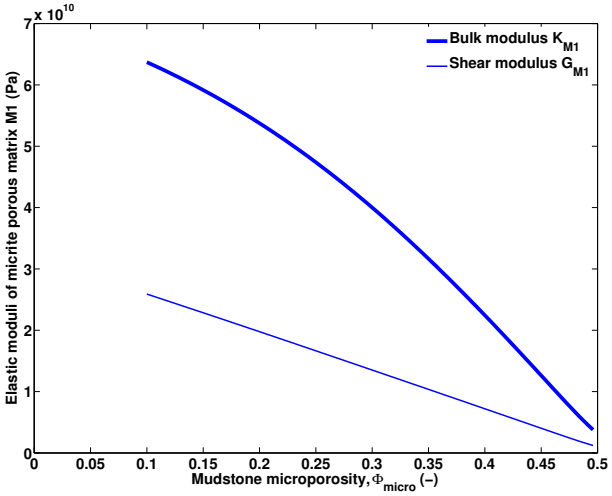

Figure 4. Elastic moduli of the porous micrite matrix in mudstone (medium M1). Initially, micropores and micrite grains are spherical. When microporosity increases due to dissolution, micropores become oblate spheroids of larger volume. Micrite grains decrease in size but remain spherical.

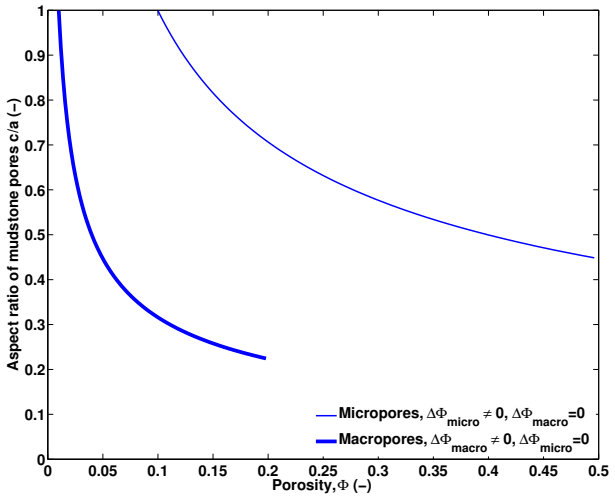

Figure 5. Evolution of the aspect ratio ($\alpha = c/a$) of the micropores (respectively macropores) at constant macroporosity (respectively microporosity) contained in mudstone. In the initial state, micropores and macro pores are spherical, with $a = b = c = 5\,\mu m$ and $a = b = c = 100\,\mu m$, respectively. When porosity increases due to dissolution, pores become oblate spheroids of larger volume: $a = b > c = 5\,\mu m$ for micropores, and $a = b > c = 100\,\mu m$ for macro pores. In the simulation, the initial volumetric fraction of the micropores (respectively macropores) was 10% (respectively 1%), in agreement to the orders of magnitude of porosity observed experimentally.

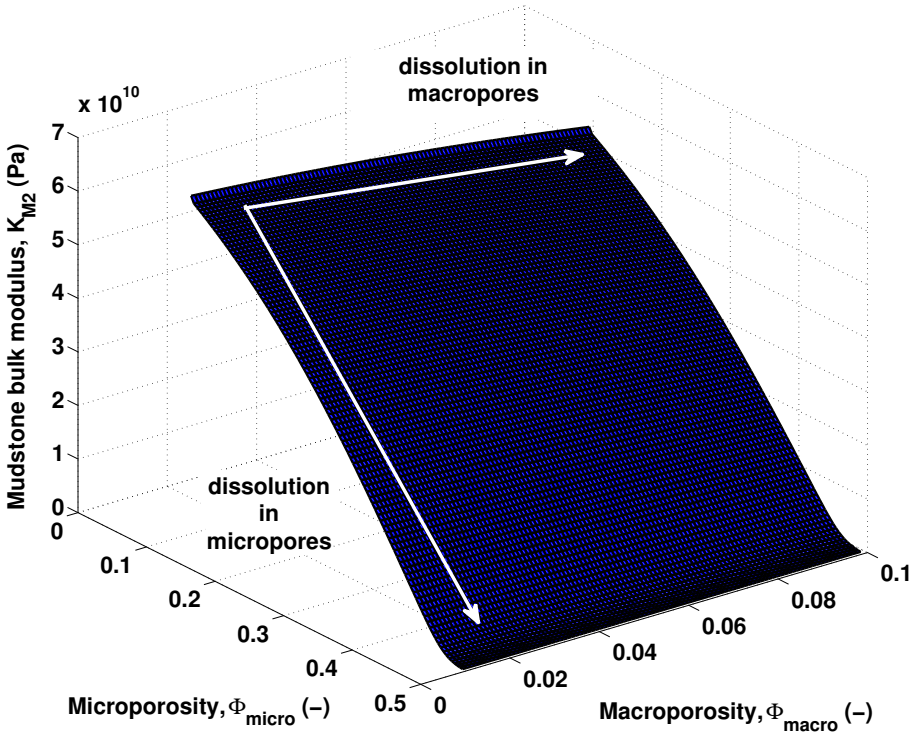

Figure 6a. Variations of the bulk modulus of mudstone with microporosity and macroporosity. Upon dissolution, the volume of pores increases and the aspect ratio of pores decreases. Micropores and macropores are randomly oriented.

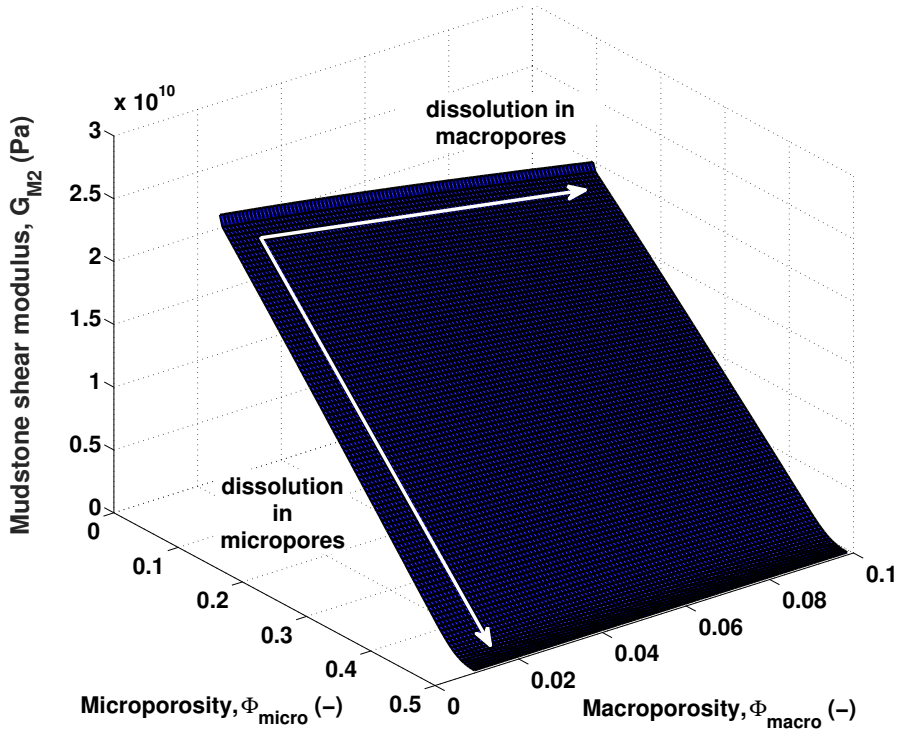

Figure 6b. Variations of the shear modulus of mudstone with microporosity and macroporosity. Upon dissolution, the volume of pores increases and the aspect ratio of pores decreases. Micropores and macropores are randomly oriented.

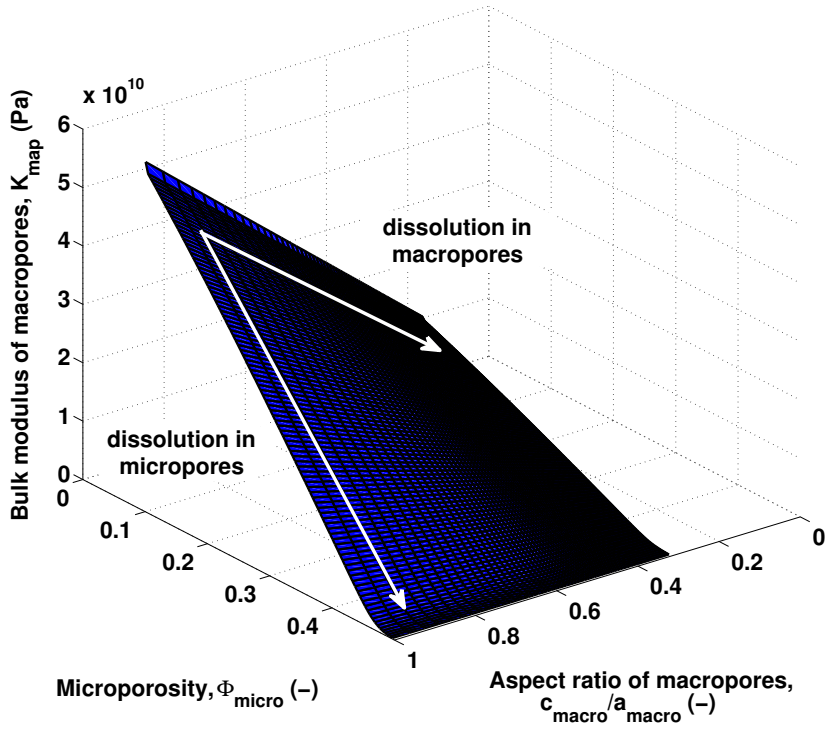

Figure 7. Variations of the bulk modulus of mudstone macropores during dissolution. Initially, pores are spheres ($a = b = c = 5\,\mu m$ for micropores, and $a = b = c = 100\,\mu m$ for macropores). Upon dissolution, pores become oblate spheroids ($a = b > c$).

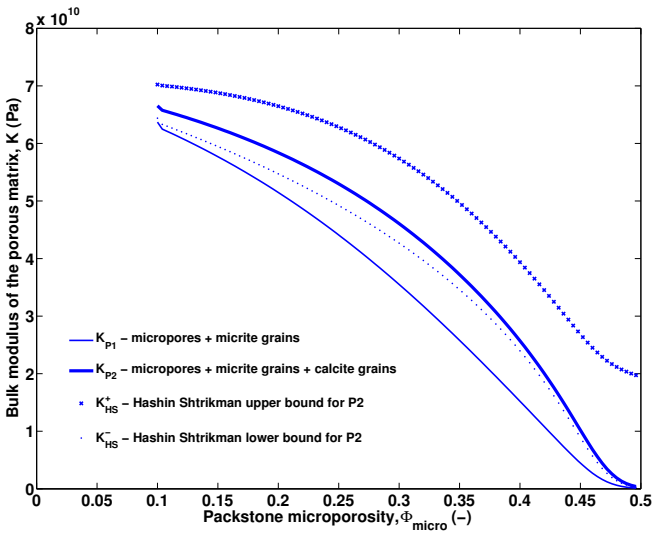

Figure 8a. Bulk modulus of the porous skeleton in packstone: micrite porous matrix (P1) and packstone skeleton (P2). The skeleton is modeled as a canvas of spherical calcite grains of constant volume fraction, and spherical elements of micrite porous matrix (medium P1) which decrease in size upon dissolution.

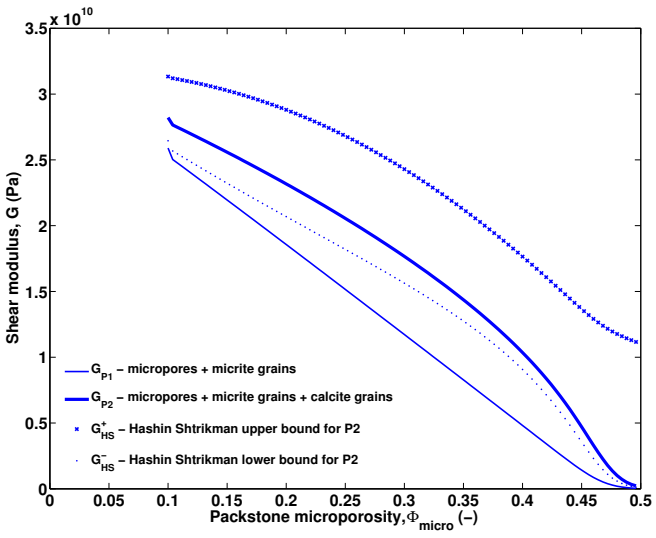

Figure 8b. Shear modulus of the porous skeleton in packstone: micrite porous matrix (P1) and packstone skeleton (P2). The skeleton is modeled as a canvas of spherical calcite grains of constant volume fraction, and spherical elements of micrite porous matrix (medium P1) which decrease in size upon dissolution.

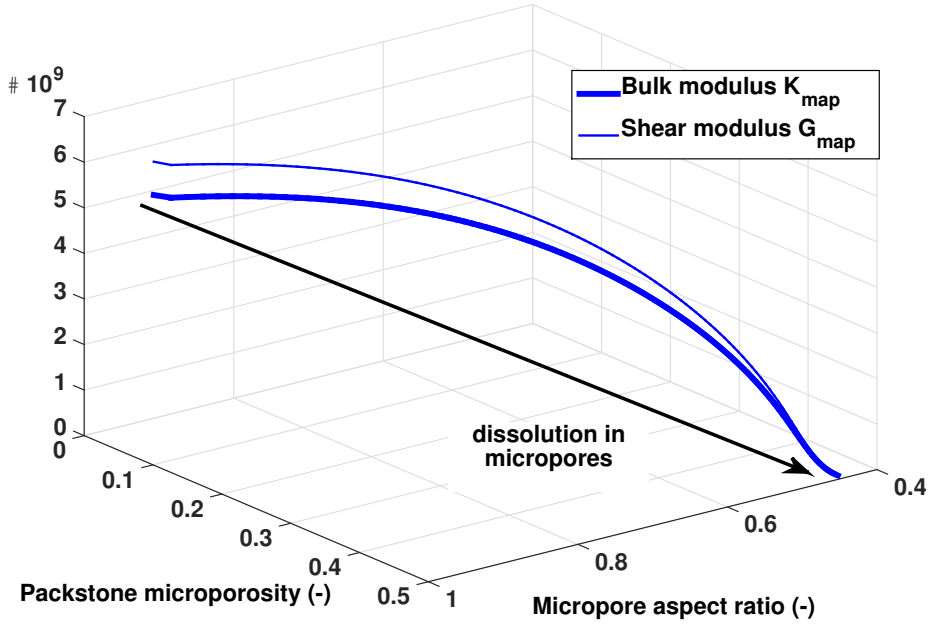

Figure 9. Evolution of macropore compressibility moduli with microporosity in packstone.

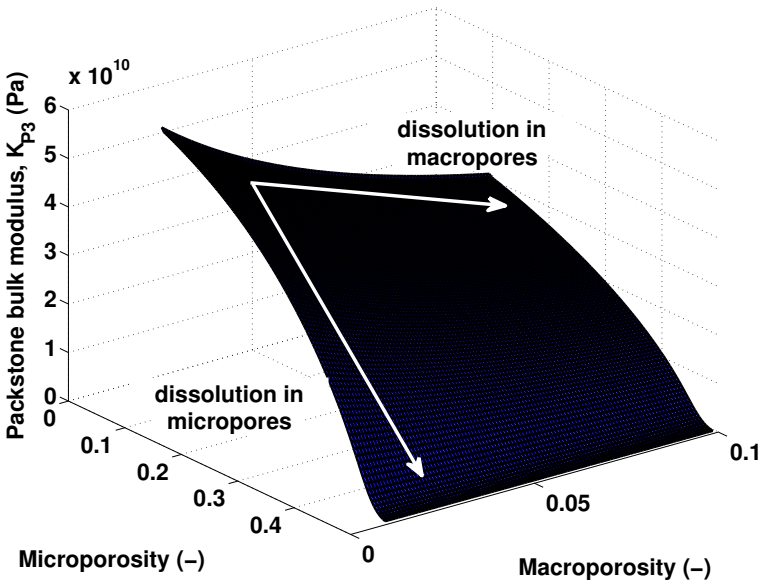

Figure 10a. Evolution of packstone bulk modulus with microporosity and macroporosity.

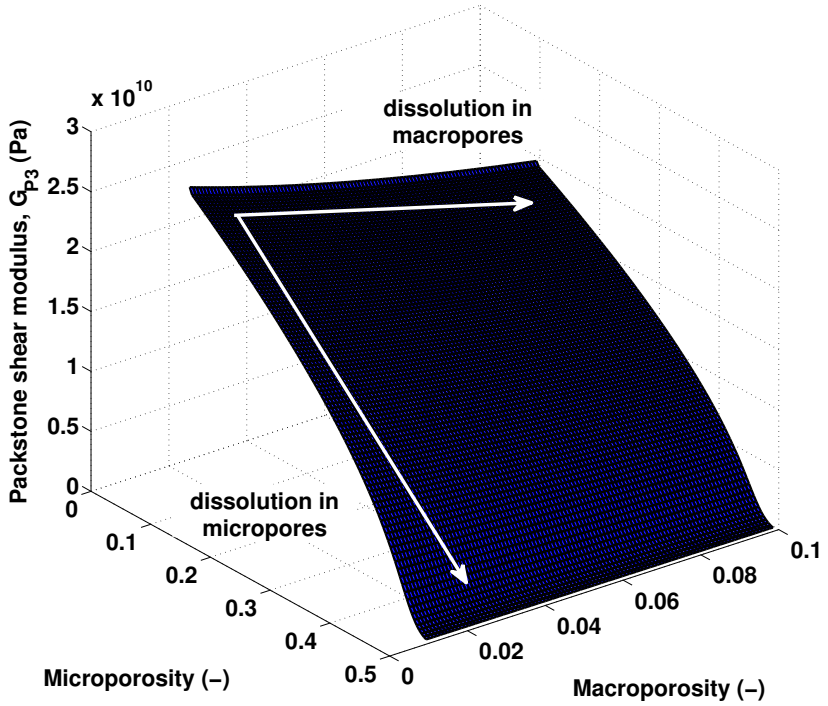

Figure 10b. Evolution of packstone shear modulus with microporosity and macroporosity.

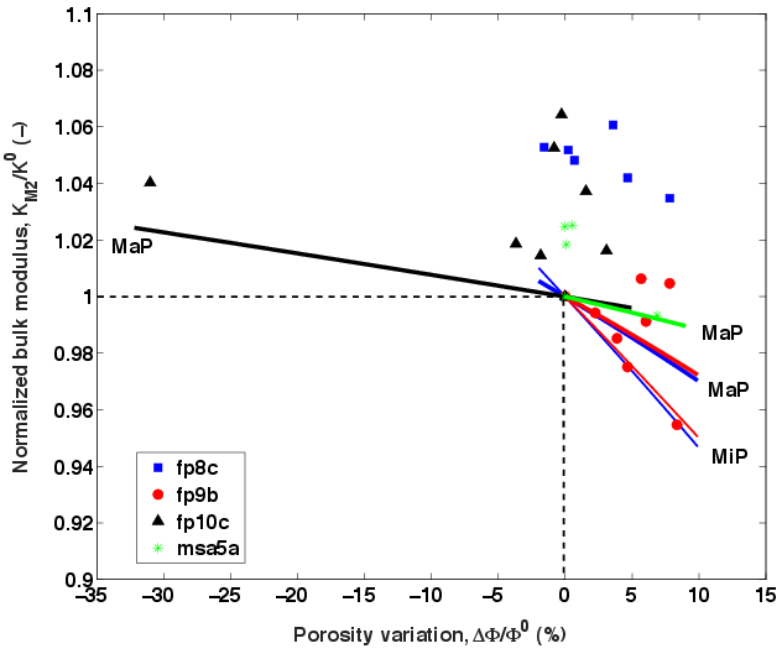

Figure 11. Evolution of mudstone bulk modulus with the variations of total porosity: measured during the injection tests (dots); predicted by the model upon changes in macroporosity (MaP) at constant microporosity (thick lines); predicted by the model upon changes in microporosity (MiP) at constant macro porosity (thin lines). Moduli were normalized with respect to the moduli of the rock in the initial state, before dissolution. Variations of the bulk modulus with macroporosity were similar to those with macroporosity for fp10c and msa5a samples. Similar trends were obtained with the model for $\Phi^0_{micro}/\Phi^0_{macro} = 0.2; 0.5; 1; 2; 5$.

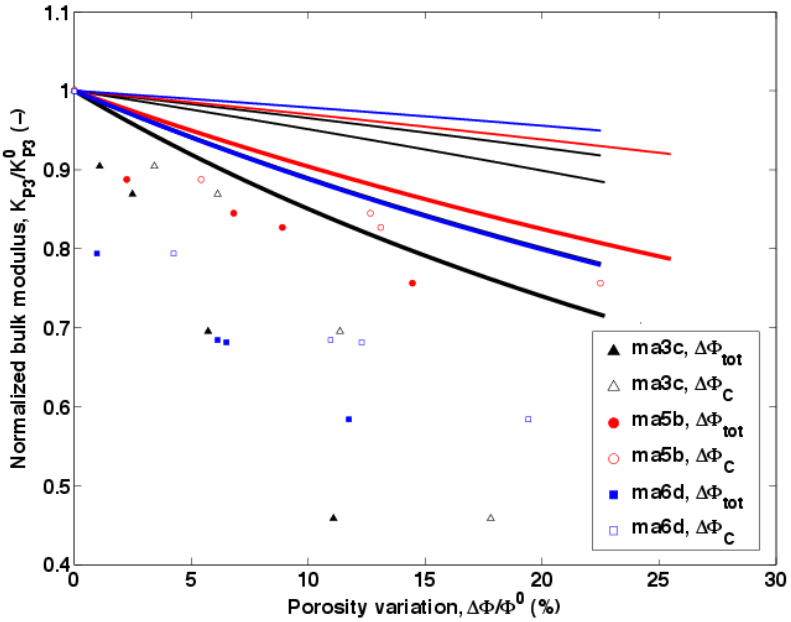

Figure 12a. Evolution of packstone bulk modulus with porosity variations: measured during the injection tests (solid dots: total porosity changes; empty dots: chemical porosity changes only); predicted by the model upon changes in macroporosity at constant microporosity (thick lines); predicted by the model upon changes in microporosity at constant macro porosity (thin lines). Moduli were normalized with respect to the moduli of the rock in the initial state, before dissolution. For ma3c sample, the simulations were done for the two initial states of porosity reported in Table 4.

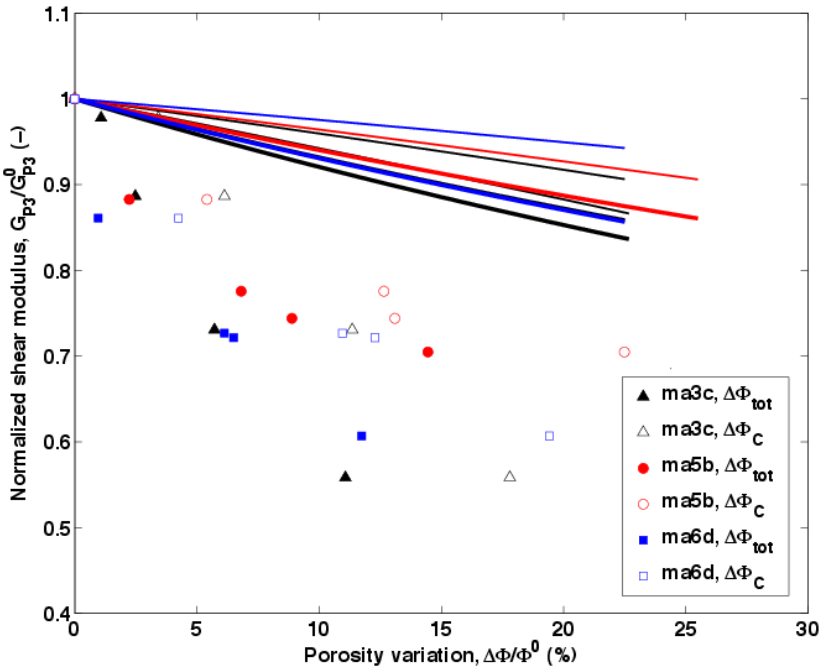

Figure 12b. Evolution of packstone shear modulus with porosity variations: measured during the injection tests (solid dots: total porosity changes; empty dots: chemical porosity changes only); predicted by the model upon changes in macroporosity at constant microporosity (thick lines); predicted by the model upon changes in microporosity at constant macro porosity (thin lines). Moduli were normalized with respect to the moduli of the rock in the initial state, before dissolution. For ma3c sample, the simulations were done for the two initial states of porosity reported in Table 4.

Table 1. List of the sample core plugs used for the experiments.

Plug Name	Formation	Rock Type	Depositional Environment	Porosity (%)	Pore Stiffness (GPa)
MSA	Monte S. Angelo	mudstone	basin to slope	0.2-10	0.08-0.6
FP	Peschici	packstone	base-of-slope to slope	0.3-15	0.02-0.1
FP	Peschici	mudstone and wackestone	base-of-slope to slope	20-40	0.02-0.1
MA	Monte Acuto	mudstone to grainstone	basin to slope	20-30	0.01-0.1

Table 2. Summary of experimental observations.

Sample	Dissolution calcite grains	Dissolution micrite grains	Compaction	Precipitation, grain welding	Porosity increase	Velocity decrease	Increase in pore stiffness
Mudstone grains $< 10\%$		✓		✓			✓
Packstone grain supported		✓	✓		✓	✓	

Table 3. Homogenization procedure to compute the bulk elastic moduli of mudstone.

Homogenization	**Step 1: Self-consistent method**	**Step 2: Self-consistent method**
	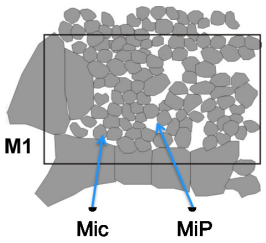	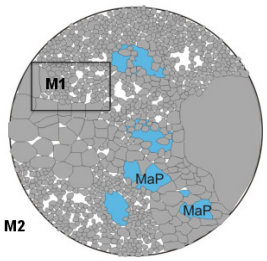
Constituent 1 (matrix)	Micrite grains (Mic): spheres that decrease in size upon dissolution $K_{(1)} = K_{CaCO3}$=71 GPa $G_{(1)} = G_{CaCO3}$= 32 GPa	Porous micrite matrix (M1): spheres that decrease in size upon dissolution and compaction $K_{(1)} = K_{M1}$ from step 1 $G_{(1)} = G_{M1}$ from step 1
Constituent 2 (inclusion)	Micro-pores (MiP): spheres that grow into oblate spheroids upon dissolution $K_{(2)} = K_{MiP}$=0 (drained) $G_{(2)} = G_{MiP}$=0	Macro-pores (MaP): spheres that grow into oblate spheroids upon dissolution $K_{(2)} = K_{MaP}$=0 (drained) $G_{(2)} = G_{MaP}$=0

Table 4. Homogenization procedure to compute the bulk elastic moduli of packstone.

Homogenization	**Step 1: Self-consistent method**	**Step 2: Self-consistent method**	**Step 3: From the expression of pore stiffness**
	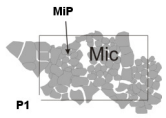	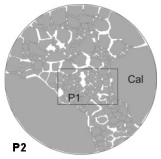	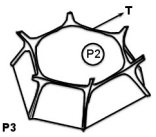
Constituent 1 (matrix)	Micrite grains (Mic): spheres that decrease in size upon dissolution $K_{(1)} = K_{CaCO3}$=71 GPa $G_{(1)} = G_{CaCO3}$= 32 GPa	Calcite grains (Cal): spheres that do not change in size upon dissolution $K_{(1)} = K_{CaCO3}$=71 GPa $G_{(1)} = G_{CaCO3}$= 32 GPa	Porous skeleton (P2) $K_{(1)} = K_{P2}$ from step 2 $G_{(1)} = G_{P2}$ from step 2
Constituent 2 (inclusion)	Micro-pores (MiP): spheres that grow into oblate spheroids upon dissolution $K_{(2)} = K_{MiP}$=0 (drained) $G_{(2)} = G_{MiP}$=0	Micrite porous matrix (P1=M1): spheres that decrease in size upon dissolution and compaction $K_{(2)} = K_{P1}$ from step 1 $G_{(2)} = G_{P1}$ from step 1	Tubular macro-pores (T), with a cross section typical of intergranular space, parametrized by a dimension and an angle of curvature $\frac{1}{K_{(2)}} = \frac{1}{K_\Phi} = \frac{13-4\nu_{P2}+8{\nu_{P2}}^2}{3(1-2\nu_{P2})}$ $\frac{1}{G_{(2)}} = \frac{1}{G_\Phi} = \frac{2(40-26\nu_{P2})}{15}$ $\nu = \frac{3K-2G}{2(3K+G)}$

Table 5. Initial carbonate microstructures tested.

Mudstones	Aspect Ratio of Micropores: 1	"fp9b" sample	$\Phi^0_{tot} = 23\%$	$\Phi^0_{micro}/\Phi^0_{macro} = 0.2; 0.5; 1; 2; 5$	
	Aspect Ratio of Macropores: 1	"fp8c" sample	$\Phi^0_{tot} = 24\%$	$\Phi^0_{micro}/\Phi^0_{macro} = 0.2; 0.5; 1; 2; 5$	
	Micropore size (c_{micro}): 5×10^{-6} m	"fp10c" sample	$\Phi^0_{tot} = 8\%$	$\Phi^0_{micro}/\Phi^0_{macro} = 0.2; 0.5; 1; 2; 5$	
	Macropore size (c_{macro}): 10^{-4} m	"msa5a" sample	$\Phi^0_{tot} = 11\%$	$\Phi^0_{micro}/\Phi^0_{macro} = 0.2; 0.5; 1; 2; 5$	
Packstones	Aspect Ratio of Micropores: 1	"ma6d" sample	$\Phi^0_{micro} = 14.4\%$	$\Phi^0_{macro} = 12\%$	$\Phi_{Cal} = 60.8\%$
		"ma5b" sample	$\Phi^0_{micro} = 10.2\%$	$\Phi^0_{macro} = 13.1\%$	$\Phi_{Cal} = 38.2\%$
	Micropore size (c_{micro}): 5×10^{-6} m	"ma3c" sample, measure 1	$\Phi^0_{micro} = 14\%$	$\Phi^0_{macro} = 12.4\%$	$\Phi_{Cal} = 43.1\%$
		"ma3c" sample, measure 2	$\Phi^0_{micro} = 19.6\%$	$\Phi^0_{macro} = 6.6\%$	$\Phi_{Cal} = 30.3\%$

Φ^0_{tot} is the total porosity before injection. Φ^0_{micro} and Φ^0_{macro} are the initial volume fractions of micropores and macropores, respectively. Φ_{Cal} is the volume fraction of calcite grains (assumed constant throughout the tests).